

Dynamical simulations of radiation damage and defect mobility in MgOB. P. Uberuaga,¹ R. Smith,^{1,*} A. R. Cleave,² G. Henkelman,¹ R. W. Grimes,² A. F. Voter,¹ and K. E. Sickafus¹¹*Los Alamos National Laboratory, Los Alamos, New Mexico 87545, USA*²*Department of Materials, Imperial College, Prince Consort Road, London SW7 2BP, United Kingdom*

(Received 24 June 2004; revised manuscript received 4 October 2004; published 3 March 2005)

Collision cascades are investigated in MgO at energies ranging from 400 eV to 5 keV. Initial energy is imparted to the principle knock-on atom in the lattice and the cascade development is tracked using classical molecular dynamics. Temperature accelerated dynamics is performed on representative defects to follow the behavior to experimental time scales. Molecular statics is used to calculate basic properties of these defects, while density functional theory calculations are used to verify the potential. In the cascades performed at the lowest energy, the lattice either reforms perfectly or, if residual defects remain, these consist of isolated interstitials and vacancies and charge-neutral Mg-O divacancies and di-interstitials. As the energy is increased to 5 keV, isolated interstitials and di-interstitials remain the most common defects but more vacancy clustering can occur and interstitial defects consisting of up to seven atoms have been observed. Molecular statics calculations find that the binding energy per atom of the interstitial clusters increases from 3.5 to over 5 eV as the size increases from 2 to 16 atoms. Long-time-scale dynamics reveal that vacancies essentially never move at room temperature but that some interstitial clusters can diffuse quickly. Although tetrainterstitial interstitial clusters are essentially immobile, there is a long-lived metastable state of the hexainterstitial that diffuses one dimensionally on the nanosecond time scale at room temperature.

DOI: 10.1103/PhysRevB.71.104102

PACS number(s): 61.72.Ji, 61.72.Cc, 61.80.Az, 61.82.Ms

INTRODUCTION

Radiation effects in materials have received much attention, both experimentally and theoretically, for a number of years. Ideally, one would like to combine the results of both to form a more detailed understanding of radiation damage. Because of the disparity in the time scales involved in each approach, however, this is often difficult to do. A typical molecular dynamics (MD) simulation of radiation damage follows the evolution of an isolated collision cascade over picosecond (ps) time scales, which is sufficient to observe the collisional phase of the cascade and to identify characteristic features of the residual defects left by the cascade process (see, e.g., Ref. 1). However, the behavior of a real material is determined not only by the number and nature of the residual defects associated with a cascade event, but also by the long-time evolution of those defects. In particular, over time scales much greater than ps, residual defects can both annihilate and aggregate. Annihilation events lead to radiation tolerance, as they remove the damage formed in the cascade; aggregation events, on the other hand, decrease the probability for annihilation and consequently exacerbate radiation damage susceptibility. To accurately predict radiation damage response in a material, it is necessary to simulate longer time scale processes such as defect mobility, annihilation, and aggregation. We recently presented theoretical results on radiation damage in MgO, where we began to bridge this time scale gap.² In this paper, we expand on that initial report, discussing in more detail our results as well as their implications.

While we are interested in the question of radiation damage in oxides in general, here we focus on the specific oxide magnesia (MgO). There are a number of reasons why we chose MgO for this initial study. First, MgO is a simple oxide and should be more amenable to study than more com-

plicated oxides. Second, MgO is a classic engineering ceramic with well-understood properties, and its radiation damage behavior has been the subject of numerous experimental and computational investigations. Finally, well established, good quality empirical potentials exist for MgO. Of course, oxides in general are very important technologically. For example, they are the conventional nuclear fuel form used in light water reactors (UO₂ and mixed oxides³) and are attractive as insulators for fusion reactor diagnostics.⁴ Also, there is growing interest in using oxides as host materials for the immobilization and long-term storage of toxic radionuclides such as the transuranics found in spent nuclear fuel.^{5,6}

The computational procedure used here consisted of four components. As detailed below, we first generated collision cascades in MgO at selected energies using MD for a few ps. We adopted representative defect configurations from the cascades and used these as starting configurations for long-time simulations via temperature accelerated dynamics (TAD).^{7,8} We also used static energy minimization to assess the relative stability of defects observed in MD or TAD simulations against alternative crystallographic arrangements of the same defect. Finally, key findings were verified using the higher-quality description afforded by density functional theory (DFT).

In this paper, we follow up on the presentation given in Ref. 2. In Sec. I, we describe the methodologies used in this study. We provide details on the molecular dynamics (MD) simulations, the molecular statics calculations, and, along with a brief description of the algorithm, the temperature accelerated dynamics (TAD) simulations. In Sec. II, we present the results of these simulations. We begin with the results of the cascade simulations performed via MD. We then apply molecular statics and TAD to representative defects found in the cascade simulations to better understand both their static and dynamic properties. We discuss the im-

TABLE I. The Buckingham parameters for the Mg-O interaction.

	r_a (Å)	r_b (Å)	ρ (Å)	A (eV)	C (eV/Å ⁶)
Mg-Mg	0.5	1.01	0	0	0
Mg-O	0.3	0.8	0.2945	1428.5	0
O-O	0.5	1.01	0.149	22764.0	27.88

plications this study has on the understanding of radiation damage in MgO, as well as some of the limitations of this work, in Sec. III. Finally, we summarize and conclude.

I. METHODOLOGY

A. Cascade simulations

The potential used in the following work is based on that given by Lewis and Catlow.⁹ It is pairwise additive and consists of two parts: an electrostatic part and a standard Buckingham term.¹⁰ For the cascade simulations, where, because of the energetic collisions, the distances between atoms can become very small, this potential was modified by adding a screened Coulomb potential for small particle separation,¹¹ smoothly joined to the outer potential so that continuous first

and second derivatives were preserved. A smooth cutoff of the Buckingham potential term at an interatomic distance greater than r_0 was also implemented. Thus calculation of the overly attractive forces for small separation and the nonelectrostatic part for large separation can be avoided.

Three different ion-ion interactions are required for this system. The Mg²⁺—Mg²⁺ interaction is purely Coulombic. For O²⁻—O²⁻, in addition to the Coulombic interaction, we use a Buckingham potential which includes a van der Waal's interaction⁹ together with an electrostatic term. For Mg²⁺—O²⁻ the van der Waal's term is assumed to be zero. The cutoff r_0 was set to 8 Å for the O—O interactions and 5.5 Å for Mg—O interactions. The original potential as given in Ref. 9 also includes a polarizable shell. In the MD and TAD simulations reported here we do not include shells, using instead a rigid-ion approximation. However, we have included shells in some of the molecular statics calculations of isolated defects for comparison and have found that they do not qualitatively change the results presented here.

As mentioned above, to avoid having a strong electrostatic attraction for close particle separation, the interactions were modeled using the Universal ZBL potential¹¹ smoothly splined to the Buckingham potential and the electrostatic term with continuous first and second derivatives. The potential for the Mg—O interactions is summarized in Eq. (1):

$$V = \begin{cases} \text{ZBL}, & r_{ij} < r_b, \\ \exp(f_1 + f_2 r_{ij} + f_3 r_{ij}^2 + f_4 r_{ij}^3 + f_5 r_{ij}^4 + f_6 r_{ij}^5), & r_b \leq r_{ij} < r_a, \\ A \exp\left(-\frac{r_{ij}}{\rho}\right) - \frac{C}{r_{ij}^6} + E_p, & r_a \leq r_{ij} < r_0, \\ E_p, & r_{ij} \geq r_0, \end{cases} \quad (1)$$

where $E_p = \pm Z_j e / 4\pi\epsilon_0 r_{ij}$ is the electrostatic term and r_{ij} is the interatomic spacing between atoms i and j . The constants in the electrostatic part have their usual meaning. The parameters for the Buckingham potential are given in Table I and those for the spline to the ZBL potential in Table II.

This model does not account for charge transfer. Specifically, we do not account for defects such as F⁺ and F centers (anion vacancies with one and two trapped electrons, respectively) in our calculations. An anion vacancy in our model is formally an F⁺⁺ center with no trapped electrons. The same is true for cation vacancies. We will discuss the implications of this on our results below.

We use the fast multipole method implemented by Rankin¹² to calculate the long-range Coulombic interactions in the MD simulations while, in the TAD simulations, we employed standard Ewald sum techniques. Although the fast multipole method has a similar scaling to the Ewald sum techniques for the system sizes studied here, it is more flexible since it does not rely on periodic boundary conditions, although periodic boundary conditions can be implemented if desired. In the implementation of the algorithm we choose not to impose periodic boundary conditions but instead to use a charge-neutral cube with charge-neutral {100} faces and embed the active part of the crystal in two fixed outer

TABLE II. The parameters for the spline to the ZBL interaction.

	f_1	f_2	f_3	f_4	f_5	f_6
Mg-Mg	14.451	-47.798	122.421	-176.000	125.130	-34.148
Mg-O	13.739	-60.640	233.169	-491.210	499.133	-196.197
O-O	-0.913	64.435	-209.550	295.875	-194.796	48.998

layers. The reason for choosing this embedded approach as opposed to periodic boundary conditions was just a matter of computational convenience. The fast multipole method is more efficient for an embedded geometry than for a periodic geometry. In principle, this geometry could result in sound waves reflecting from the boundaries, though similar issues would exist for periodic boundary conditions. In fact, for MgO, because the barriers for diffusion are typically high relative to the energy in any reflected wave, we expect little to no impact from the fixed boundaries. A few tests in which we thermalized the boundary layers resulted in very similar results. However, we have also taken care in choosing the sizes of our simulation cells, as will be addressed below. All cascade simulations were carried out at an initial temperature of 0 K.

Previous MD work has indicated¹³ that the displacement energy threshold in MgO is very high: about 65 eV for an O primary knock-on atom (PKA) and about 90 eV for the Mg PKA. We obtain similar values with this potential.

Primary knock-on atoms at energies of 400 eV, 2 keV, and 5 keV were investigated. The small value of 400 eV was chosen to investigate the types of defects that form when the energy is near the displacement threshold, where the defects are expected to be small in number. Values larger than 5 keV require more computational resources and have not been studied at this time. Trajectories were evenly distributed between PKAs of both O and Mg and run for up to 8 ps, or until the defects had thermalized. Initial trajectory directions were randomly distributed over a solid angle representative of the crystal symmetry. In total 20 trajectories were run at 400 eV, and 12 each for the 2 keV and 5 keV PKA. The actual simulations consisted of imparting a kinetic energy of either 400 eV, 2 keV, or 5 keV to the primary knock-on atom. The dynamics of the system with this extra kinetic energy were evolved in time using standard molecular dynamics techniques including the velocity Verlet algorithm for time integration, linked neighbor lists to achieve order N scaling, and a variable time step dependent on the maximum kinetic energy in the system; see Ref. 14 for details.

A word should be said about the size of the systems studied. These varied from 4000 to 160 000 atoms depending on the size and extent of the cascade. We verified that the atoms displaced by the cascade were sufficiently far away (at least four nearest-neighbor distances) from the outer boundary of the embedded geometry, thus ensuring that effects due to interaction with the boundary were minimal. In the 400 eV cascades, the maximum kinetic energy imparted to atoms near the boundary was only 0.05 eV, too small to activate migration in this system. The cells do tend to heat up because of the added energy. For example, in the case of the 400 eV PKAs, the temperature of the system increased to about 370 K. This could accelerate the recombination process, compared to $T=0$ K, but in a way that should be consistent with a system at finite temperature. We are interested in longer-time dynamics at $T=300$ K, so the systems that went above $T=300$ K could bias the results slightly, but the acceleration of events for a few ps at this higher T is probably negligible. For the higher energy cascades, there was less heating of the system, leading to final temperatures below $T=300$ K.

B. Temperature accelerated dynamics

To follow the long time behavior of the defects seen in the cascade simulations, temperature accelerated dynamics was applied to representative defect structures. TAD^{7,15} is one of a number of accelerated molecular dynamics techniques⁸ that allow for the simulation of much longer time scales than conventional MD. The TAD algorithm involves running MD at a high temperature T_{high} , typically much higher than the temperature of interest T_{low} , in a way that constrains the dynamics to the current state of the system (referred to as basin constrained MD, BCMD). The times of events seen at this high temperature are extrapolated to times at T_{low} . The BCMD procedure is continued until the stopping criteria is met. This stopping criteria depends on two parameters— δ , the uncertainty of missing an event and ν_{min} , an assumed minimum prefactor in the system. These two parameters thus control the accuracy of a TAD simulation. Once the stopping time has been reached, the event that occurs earliest at T_{low} is then accepted and the entire process repeated in the new state. The extrapolation of event times from T_{high} to T_{low} is exact if harmonic transition state theory holds for the system being studied at both temperatures. It requires knowledge of the energy barrier for the event, which we find using the nudged elastic band method.^{16,17}

A critical requirement of the TAD algorithm is detecting transitions from the current state. In these simulations, a transition was declared if, upon minimization, any atom had moved more than 0.25 Å from the minimum of the current state.

The system sizes that can be studied with TAD are smaller than those accessible with conventional MD. In the work described here, TAD was applied to representative defects observed to form in the larger MD simulations, but in a reduced system size containing 512 ions in a periodic cell. A few simulations on periodic cells containing 1728 atoms were performed to ensure that effects due to periodic boundary conditions were not significant, which was indeed the case for the simulations reported here.

In MgO, the barriers for different defects to diffuse vary greatly, ranging from 0.3 to over 2 eV. To enhance the speed of the TAD simulations, we have employed a recently developed extension to TAD that incorporates the dimer method.¹⁸ This so-called dimer-TAD algorithm¹⁹ uses the dimer method to find the minimum barrier to leave the state. This minimum barrier is then used to redefine the time at which the BCMD can be stopped, often reducing it dramatically. This new stopping criteria no longer depends on δ and ν_{min} . Instead, it depends on the minimum barrier in the system. This new TAD algorithm also allows us to tune T_{high} for the current state based on the minimum barrier, resulting in typical values between 300 and 2000 K. In the simulations reported here, we used $T_{\text{low}}=300$ K. We performed ten dimer searches per state, focused on the “active” region of the system, or that part of the system in which interstitials or vacancies resided. We can never be 100% certain that the dimer searches have found the lowest barrier for escape from the state. In the simulations reported here, the BCMD found a lower barrier than the dimer searches about once per 17 escapes. When this occurred, the difference between the dimer-

found minimum barrier and the lower discovered barrier was usually small, on the order of 0.05 eV or less. Such errors would affect the time scales over which the simulations occurred and the particular events a simulation followed, but the final structures and their migration barriers reported here are likely unaffected.

For consistency with the molecular statics calculations described below, which were performed at the minimum-energy lattice constant of the potential, all TAD simulations were also performed at the fixed volume corresponding to this minimum-energy lattice constant. Although the finite-temperature TAD simulations were thus under pressure, the temperature dependence of each activated process at $T=300$ K (as well as at the higher temperature used in TAD) is given by the same barrier height computed in the molecular statics.

Finally, investigating charged defects is more computationally challenging than neutral defects. This is because a net charge resides within the simulation cell, so standard Ewald techniques and periodic boundary conditions are no longer applicable and the Coulomb sum is instead done directly on cells with free boundaries. Such cells require a layer of frozen material at the boundary with a thickness equal to the cutoff of the potential which, in turn, results in cells that are much bigger. For the charged tri-interstitial defects investigated in the TAD simulations reported below, we used a cell containing 1728 atoms, within which 512 atoms were allowed to move. (The skin size was chosen to be one unit cell in each direction. For example, the 512-atom interior consists of the 8 atom unit cell replicated 4 times in each dimension. The total cell is thus the unit cell replicated 6 times in each direction, so that the moving interior has a skin of one unit cell on each face.) We performed tests with even larger cells on key barriers and found that this size gave values to within 0.05 eV of the converged values.

C. Molecular statics

In the molecular statics calculations, the perfect lattice structure and energy is determined by starting with the experimental values and adjusting both ion positions and lattice vectors, using the Newton-Raphson minimization procedure, until each ion experiences close to zero force (the short-range parameters were chosen to reproduce the lattice structure very closely). The internal energy of a defect, or a cluster of defects, can then be calculated via the Mott-Littleton approximation.²⁰ This begins with the relaxed perfect lattice, which is partitioned into spherical concentric regions. A defect is then placed in the center of region I. All ion positions in region I are allowed to relax in response to the defect, and interactions are summed over all pairs of ions within this region. Here the radius of region I is limited to 12.1 Å since the calculated defect energies remain constant at increased radius values, i.e., the defect energy has converged with respect to region size. The outer region II extends to infinity and responds to the defect as a dielectric continuum according to the Mott-Littleton approximation. To ensure a smooth transition between regions I and II, an interfacial region IIa, of radius 32.9 Å, is introduced. Ion positions within region

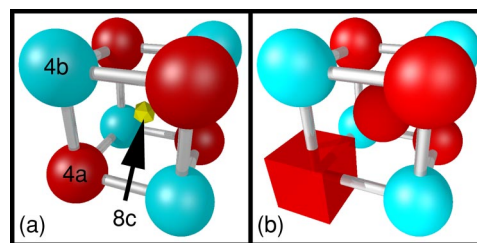


FIG. 1. (Color online) (a) The basic structure of the MgO crystal. O atoms (dark/red color) occupy the 4a Wyckoff sites and Mg atoms (light/blue color) occupy the 4b Wyckoff sites of the two interpenetrating tetrahedra. The interstice site lies in the middle of this repeating unit, in the 8c site (represented by the octahedron). (b) Structure of the most elementary Frenkel pair, in which one of the atoms is removed from a lattice site (represented by the cube) and placed in the 8c site. This structure is not stable in MgO. The Frenkel pair must be separated by four nearest-neighbor sites before it is stable.

IIa are allowed to vary, subject to forces determined via the Mott-Littleton approximation; however, the interaction energies between region I and II ions are calculated explicitly. Here calculations are carried out using the code CASCADE.²¹

These perfect lattice calculations are referred to as “static” since vibrational entropy contributions are not included in the model. The energies calculated therefore relate, via the quasiharmonic approximation, to the temperature of the lattice to which the potential parameters were fitted, in this case, room temperature. For further details see Ref. 22. Because we are interested in room temperature in this study, we kept our systems at the minimum-energy lattice constant predicted by this potential.

II. RESULTS

A. MD simulations for large systems and picosecond time scales

MgO belongs to the space group $Fm\bar{3}m$. The structure of the basic repeating unit, shown in Fig. 1(a), consists of two interpenetrating tetrahedra in which O atoms are placed on the corners of one tetrahedron, in the 4a Wyckoff sites, and Mg atoms are in the corners of the other tetrahedron on 4b sites. The interstices of this structure lie in the center of this octant of the unit cell, or on the 8c sites. Figure 1(b) shows the structure of the simplest Frenkel pair for this system in which one of the atoms is removed and placed in the 8c site. In MgO, this particular configuration of the Frenkel pair is not stable—it collapses to the perfect crystal.

Figure 2 shows a typical cascade simulation in MgO for a PKA energy of 400 eV. At $t=0$, the initial knock-on event occurs. Very quickly, the damage saturates ($t=80$ fs) and settles ($t=260$ fs), after which only a few isolated defects remain. In this particular case, these defects consist of two vacancies and two interstitials, one of each type [Fig. 2(b)]. Due to the strong electrostatic attraction between the oppositely charged interstitials, they move toward one another and by $t=6.5$ ps they have combined to form an MgO di-interstitial [Fig. 2(c)].

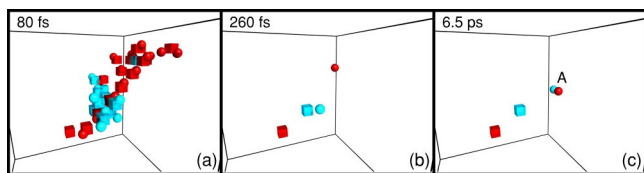


FIG. 2. (Color online) The defects in a cascade generated from a 0.4 keV O PKA. The color scheme, used in this and all subsequent figures, is dark (red) for O defects and light (blue) for Mg defects. Spheres indicate interstitials, or atoms more than 0.8 \AA from a lattice site, and cubes indicate vacancies, or lattice sites with no atom within 0.8 \AA . (a) At $t=80 \text{ fs}$, the number of displaced atoms peaks. (b) By $t=260 \text{ fs}$, most of the defects have recombined and only a few isolated defects remain. (c) By $t=6.5 \text{ ps}$, the interstitials have formed a di-interstitial (labeled A). Taken from Ref. 2.

Figures 3 and 4 illustrate other scenarios occurring for 400 eV. In Fig. 3, as in Fig. 2, after the initial cascade has settled, a Mg interstitial is situated one lattice spacing from a Mg vacancy. In contrast to the simulation of Fig. 2, in which the Mg interstitial combines with an O interstitial to form a stable di-interstitial, in the case of Fig. 3, the O interstitial hops toward the Mg interstitial to form a di-interstitial which is still very close to the original Mg and O vacancies and soon annihilates with them. Whether the interstitial annihilates with a vacancy, as shown in Fig. 3, or aggregates with another interstitial depends on the complex electric field created by all of the defects in the vicinity.

In another simulation, illustrated in Fig. 4, an O interstitial is formed $\sim 15 \text{ \AA}$ from the vacancy. In many cases, interstitials that were this far away from a vacancy were stable over

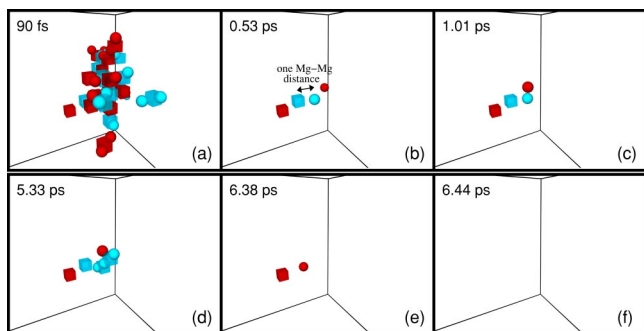


FIG. 3. (Color online) Recombination events in a cascade generated by a 400 eV PKA in MgO. Spheres indicate interstitials, or atoms more than 0.8 \AA from a lattice site, and cubes indicate vacancies, or lattice sites with no atom within 0.8 \AA . (a) The peak number of displacements at 90 fs. (b) 0.53 ps where most of the defects have recombined. At this stage the Mg interstitial is only 1 lattice unit from the Mg vacancy. Normally, this would be an unstable position for the Mg interstitial, but the nearby O interstitial and O vacancy act to partially cancel the attractive pull of the Mg vacancy, stabilizing the Mg interstitial in this position. (c) After 1.01 ps an MgO di-interstitial forms. (d) The Mg atom in the di-interstitial recombines with the nearby vacancy after 5.33 ps (the large number of objects present in this figure illustrate the number of atoms involved in the process). (e) The remaining O atom hops closer to the remaining O vacancy after 6.38 ps. (f) The final event leading to complete recombination occurs after 6.44 ps.

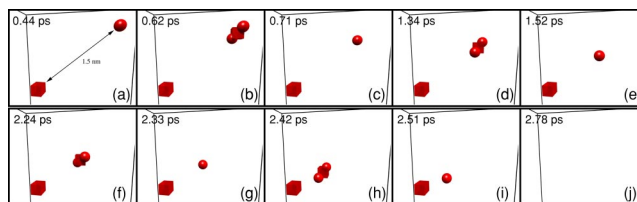


FIG. 4. (Color online) The recombination of an O^{2-} interstitial, generated from a 400 eV O PKA, with an O vacancy. (a) 0.44 ps after the start of the cascade, by which time the cascade has settled, leaving an isolated interstitial and vacancy separated by 1.5 nm. (b) Motion via the $\langle 111 \rangle$ interstitialcy event after 0.62 ps. (c) Interstitial moves to a new $8c$ site, 1.26 nm from the vacancy after 0.71 ps. (d) Motion via the same $\langle 111 \rangle$ mechanism to new site after 1.34 ps. (e) 0.9 nm from the vacancy after 1.52 ps, (f) 2.24 ps, and (g) 0.68 nm from the vacancy after 2.33 ps; (h) 2.42 ps, (i) 2.51 ps, (j) The event leading to final recombination occurs after 2.78 ps. The last recombination event occurs quickly, appearing as a two-stage hop and not directly via the $\langle 111 \rangle$ mechanism. However, further analysis reveals that events such as these are really one event, characterized by one saddle point (see the discussion in Sec. II C).

picosecond time scales. However, in this particular case, perhaps because of the residual thermal energy from the PKA event ($T=370 \text{ K}$, as discussed above), the interstitial jumps to the vacancy site and recombines. The main mechanism is to move between $8c$ sites [see Fig. 1(a)] in the $\langle 111 \rangle$ direction via a collinear interstitialcy mechanism, in which the interstitial in one $8c$ site replaces a lattice atom which simultaneously moves to another $8c$ site. This is in agreement with the prediction of Ref. 23.

In general, for the 400 eV PKA, only a small number of defects form due to a tendency for nearby defects to recombine over the time scale of a few picoseconds. Indeed, previous work on MgO has shown that Frenkel pairs are stable only if the separation is greater than the fourth-nearest-neighbor distance.²³ As seen in the snapshots from the three cascades shown in Figs. 2–4, the only defects observed were isolated vacancies, isolated interstitials or di-interstitial pairs where an Mg and an O atom were situated at adjacent $8c$ sites so that the di-interstitial axis was always parallel to the cell edges, or in $\langle 100 \rangle$ directions. In only one case at 400 eV was a divacancy formed.

The results of all of the cascade simulations are summarized in Table III. The lattice completely or very nearly completely reannealed within 8 ps of the impact event in 13 of the 20 trajectories investigated at 400 eV. In four simulations a single Frenkel pair formed that was sufficiently well separated—by at least 1 nm—so that it had not moved at all over the 8 ps time scale. MgO di-interstitials formed three times. These di-interstitials were stable over the 8 ps time scale when separated by more than 2 lattice units (1 lattice unit = 4.1986 \AA with the Lewis and Catlow potential) from a nearby vacancy. Summarizing all of these simulations, we saw about one Frenkel pair formed for every two simulations. However, the number of atoms displaced from their original lattice sites and moved to others is about twenty times larger, averaging about 9 per trajectory.

When the PKA energy is increased, the same types of defects seen at 400 eV still predominate, typically separated

TABLE III. The total number of Frenkel pairs and principal defect types (monointerstials and di-interstitials and monovacancies and di-vacancies) for PKA energies of 0.4, 2, and 5 keV remaining after the collisional phase ($t=8$ ps) of a cascade. In addition, one tri-interstitial formed at 2 keV and 4 tri-interstitials, one tetrainterstitial, and one 7-interstitial cluster formed at 5 keV. Taken from Ref. 2.

PKA energy (keV)	No. of trajs.	number of defects					perfect lattice
		Frenkel pairs	monoint. O/Mg	monovac. O/Mg	di-int	di-vac	
0.4	20	10	3/1	5/3	3	1	13
2	12	84	21/24	33/30	15	6	0
5	12	216	57/62	78/80	39	15	0

by much larger distances, though some clustering of defects also begins to occur. Figure 5 shows examples of this for two typical cascades at 2 keV. As in the case of 400 eV cascades, the di-interstitial pairs form not by direct collision but rather over picosecond time scales due to the strong Coulomb interaction between nearby interstitials. The vacancy clusters, however, form during the collisional phase of the cascade and are immobile. Indeed, in all of the simulations we have performed at all energies, we have never seen a vacancy move during the 8 ps collisional phase. At 2 keV, an average of 7 Frenkel pairs remain after 8 ps with an average of 48 atoms displaced from their initial lattice sites. In 12 trajectories, 15 MgO di-interstitials formed in addition to 20 isolated O and 20 isolated Mg interstitials. Out of the 12 trajectories, a single O-Mg-O tri-interstitial also formed, which, like the di-interstitial, consisted of linear interstitials located at adjacent $8c$ sites parallel to a unit cell axis. There were also a few examples of vacancy clusters. Specifically, five divacancies and one trivacancy cluster were observed.

One interesting observation at all energies was that trajectories initiated in either $\{110\}$ or $\{100\}$ planes, irrespective of direction, produced defects which were confined to the original plane of propagation or one lattice unit on either side. The defect clusters of size three and larger observed in the cascades occurred generally for PKA atoms initiated in these low index planes.

Typical defect distributions at the end of a 5 keV cascade are shown in Fig. 6. At this energy, an average of 18 Frenkel pairs survived after 8 ps of simulation time, with an average

of 124 displaced atoms produced in the collisional phase of the cascade per trajectory. Compared to lower energy cascades, while isolated defects still predominate, there is evidence of more defect clustering. Out of the 12 trajectories simulated, 62 Mg interstitials and 57 O interstitials survived. In addition to these isolated interstitials, there were 39 MgO di-interstitials—an average of more than 3 per cascade—and 4 tri-interstitials, two each of O-Mg-O and Mg-O-Mg. Both of these tri-interstitial structures had the same linear structure. In one case an interstitial cluster of 4 atoms formed and in another case we saw a cluster containing 7 interstitial

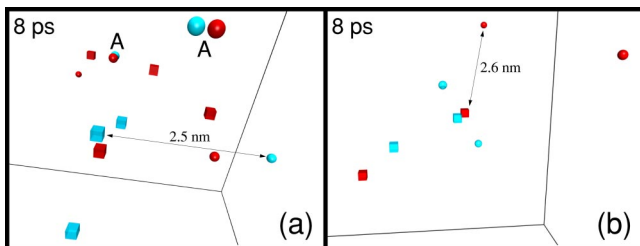


FIG. 5. (Color online) Examples of the spread-out residual damage after the collisional phase of the cascade at 2 keV. (a) The image shows three separated Mg vacancies and four O vacancies. There are two MgO di-interstitials (labeled A), one Mg interstitial, and two O interstitials. (b) In this case, only well-separated monointerstials and vacancies occur.

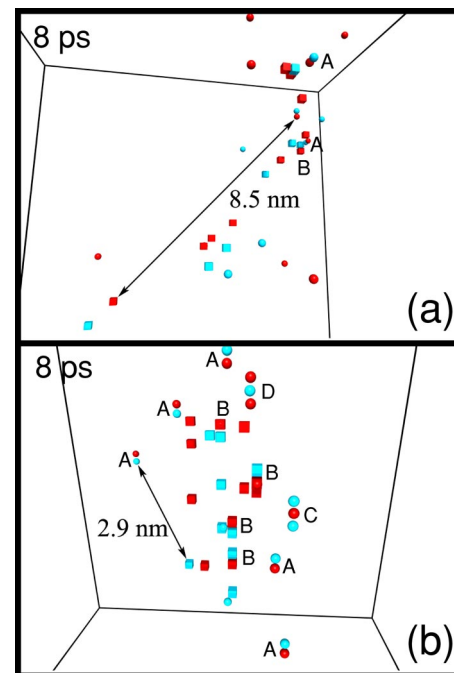


FIG. 6. (Color online) Typical defects remaining after 8 ps for a PKA energy of 5 keV. Defects are labeled as (A) di-interstitials, (B) divacancies, (C) Mg-O-Mg tri-interstitials, and (D) O-Mg-O tri-interstitials. (a) The image shows two MgO di-interstitials and one divacancy in addition to isolated interstitials and vacancies. (b) In this case the cascade is more compact and there are four divacancies in addition to five di-interstitials, two tri-interstitials, three O interstitials, and one Mg interstitial. The distance between the two tri-interstitials is 1.9 nm. The length of each side of the cubic simulation cell, shown for perspective purposes, is 11.9 nm.

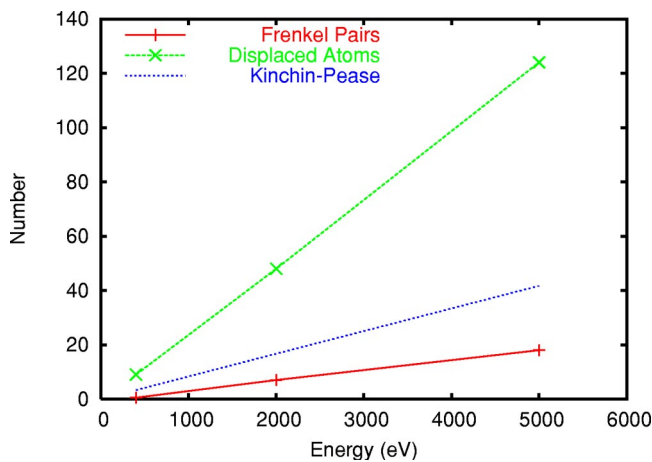


FIG. 7. (Color online) The number of defects and displaced atoms as a function of PKA energy. The displacement energy threshold for the Kinchin-Pease formula was taken as $E_D=60$ eV. The lines are guides for the eye.

atoms. Clustering of vacancies was also more prevalent: 15 divacancies, 6 trivacancies, and one case of an 8 atom vacancy cluster were observed. For the 2 and 5 keV cascades, the isolated interstitials do not so readily recombine with nearby vacancies in the collisional phase of the cascade compared to the 400 eV cascade. This is probably due to the longer distances between vacancies and interstitials and the complex Coulomb field due to the larger number of defects formed.

Over the energy range 400 eV to 5 keV, there is an almost linear dependence with energy for both the total displaced atoms and the number of residual Frenkel pairs, as shown in Fig. 7. Assuming a displacement energy threshold E_d of 60 eV, the number of Frenkel pairs remaining after the cascade for all three energies is about 45% of the Kinchin-Pease value, similar to the result for metals.²⁴

Finally, in addition to an increase in both the number of residual Frenkel pairs and the maximum number of Frenkel pairs produced during the cascade with PKA energy, the time at which the damage peaks also increases. This is illustrated in Fig. 8. The average time of peak damage increases from 82 fs at 400 eV to 126 fs at 5 keV.

B. Defect energies via molecular statics

The binding energy of isolated small interstitial clusters and vacancies was examined using static energy minimization via a Mott-Littleton approach similar to that used in Ref. 25 and compared to those occurring at the end of the cascades. Here, we have defined the binding energy as $E_{\text{isolated defects}} - E_{\text{cluster}}$. The results for the most stable configurations are shown in Table IV. Some of these results have been previously reported in Ref. 2. In addition to those results, we have calculated the binding energy for clusters containing 12, 14, and 16 interstitials. The binding energy increases from 3.49 eV per atom for the Mg-O di-interstitial to about 5.2 eV per atom for clusters containing 10 or more interstitials. Although the isolated interstitials at the 8c site were found to be the most stable configuration, $\langle 110 \rangle$ split

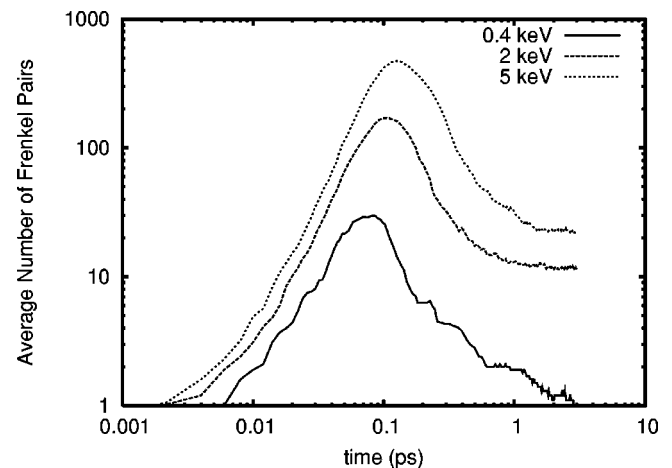


FIG. 8. The average number of Frenkel pairs versus time in cascades with PKA energies of 400 eV, 2 keV, and 5 keV. The average time of peak damage increases with PKA energy, as does both the peak number of Frenkel pairs and the number of residual Frenkel pairs.

interstitials of both types—Mg and O—were also found to be stable, but higher in energy by over 0.5 eV. The energy barrier for this metastable structure to decay to the 8c structure is very small—less than 0.01 eV—and consequently these were never observed in the collision cascades. In contrast the energy barrier for migration of O^{2-} between 8c sites was found to be 0.40 eV and for Mg^{2+} it was 0.32 eV.

While we find the 8c site to be most stable for a charged interstitial, others have found that this is not the most favorable site for the *neutral* interstitial. Different electronic structure calculations find either the O $\langle 111 \rangle$ split interstitial²⁶ or the O $\langle 110 \rangle$ split interstitial²⁷ as the most stable neutral interstitial. While the source of the discrepancy between these two studies is not clear, it may at least be partially due to differences in cell size.²³ In our study, because of the limitations of our model, the interstitial is fully charged and prefers the 8c site.

TABLE IV. The energy of the most strongly bound isolated small clusters in MgO found to date, up to size 8. The structures of the clusters containing 6 and 8 interstitials are shown in Fig. 9.

No. in cluster	defect type	geometry	energy (eV)	binding energy (eV/atom)
1	Mg_i	cell center	-10.63	
1	O_i	cell center	-11.90	
1	Mg_v		+24.73	
1	O_v		+25.47	
2	$(MgO)_i$	$\langle 100 \rangle$	-29.50	3.49
2	$(MgO)_v$	$\langle 100 \rangle$	+46.85	
3	$(MgOMg)_i$	$\langle 100 \rangle$	-43.96	3.60
3	$(OMgO)_i$	$\langle 100 \rangle$	-45.17	3.58
4	$(2Mg2O)_i$		-62.46	4.35
6	$(3Mg3O)_i$		-95.61	4.79
8	$(4Mg4O)_i$		-129.71	5.03

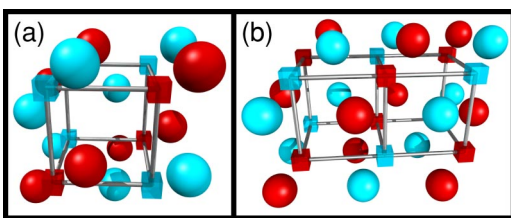


FIG. 9. (Color online) Ground-state structure of the (a) hexainterstitial and the (b) octainterstitial. The hexainterstitial is centered around one MgO fundamental structural unit (the bars and vacant lattice sites, represented by cubes) while the octainterstitial extends over two structural units. Each of the bars connecting the vacant sites lies along a $\langle 100 \rangle$ direction. In the hexainterstitial structure, six atoms have been inserted into the basic MgO structural unit, displacing the crystallographic atoms away from their lattice sites. The octainterstitial exhibits a similar structure in which eight atoms have been inserted into two MgO structural units.

As discussed below, the TAD simulations have revealed the ground state structure for the hexainterstitial and octainterstitial clusters. Shown in Fig. 9, the structure of the ground-state octainterstitial is an extended version of that of the hexainterstitial. This suggests that extended interstitial defects can be created by adding the basic building block seen in the hexainterstitial cluster, that is, a compact MgO di-interstitial pair. This common structural motif was extended to build interstitial clusters containing more than eight interstitials. All of these proved stable when relaxed, except for the dodecainterstitial cluster. In this case, the relaxation involves a twisting of the end of the cluster so that this end lies along a new $\langle 100 \rangle$ direction, forming an “L-shaped” structure in which each branch is composed of the motif seen in the hexainterstitial. This structure has a slightly higher binding energy than those of the neighboring interstitial cluster sizes. We have yet to determine what impact this structure has on the mobility of the dodecainterstitial cluster or if other cluster sizes also exhibit this lower energy structure.

We emphasize that we do not know for certain if the structures investigated for the larger cluster sizes are indeed the ground state structure, and the fact that the dodecainterstitial cluster exhibits a different structure suggests that it is very possible that even more compact structures will be more stable. However, as the number of possible cluster geometries grows exponentially with cluster size, it is very difficult to explore the structure space fully. The trends discussed here are not necessarily definitive. Even if these extended $\langle 100 \rangle$ structures are not the ground state, they are still very stable structures. Experimentally, under certain conditions, interstitial dislocation loops in MgO are seen to grow preferentially in the $\langle 100 \rangle$ direction and the defect clusters we see here may be precursors to the dislocation loops seen in experiment. However, more work needs to be done before any definite comparisons can be made.

C. Long time behavior via temperature accelerated dynamics

The cascade simulations described above can only follow the dynamics of the resulting defects for time scales on the

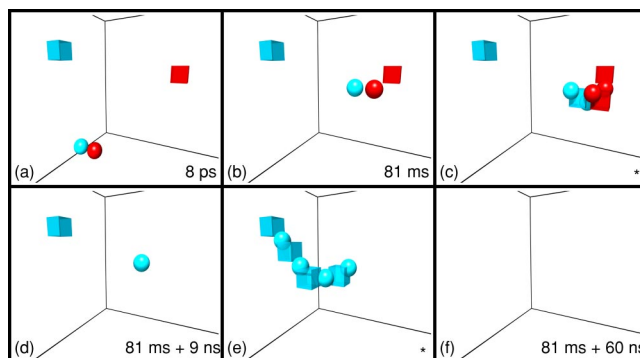


FIG. 10. (Color online) Results of a typical TAD simulation. (a) The initial configuration contains a di-interstitial and two vacancies, similar to the final state of Fig. 2(c). (b) By $t=81$ ms, the di-interstitial has diffused toward the O vacancy and, (c) via a concerted event involving several atoms, (d) the O atom of the di-interstitial annihilates the O vacancy 9 ns later. The remaining Mg interstitial then recombines with the Mg vacancy via a long-range, concerted mechanism involving many atoms (e) which results in the reformation of the perfect crystal (f) 51 ns after the first annihilation event. The asterisks indicate structures interpolated between the initial and final states of the events. See the text for discussion on the details of the event.

order of ps. To truly understand the behavior of these defects, longer times must be simulated. We applied TAD to representative defect structures seen in the cascades to achieve experimental time scales.

Figure 10 shows results from a long-time scale TAD simulation of the annealing, at 300 K, of the typical damage seen at 400 eV. The initial configuration is very similar to that seen in Fig. 2(c), consisting of two isolated vacancies and a di-interstitial. At 300 K, vacancies are immobile even on the time scale of centuries. In contrast, an isolated MgO di-interstitial, moving in $\langle 111 \rangle$ directions via a collinear interstitialcy mechanism, diffuses on the time scale of tenths of seconds with a barrier of 0.75 eV. In the presence of the vacancies, because of the strong electrostatic interactions, this barrier is reduced so that by $t=0.08$ s, the di-interstitial reaches the O vacancy and partly annihilates with the vacancy. The remaining Mg interstitial quickly (within 51 ns) finds the Mg vacancy, completing the annealing process and resulting in a perfect crystal.

The annihilation event shown in Fig. 10(e) is an interpolation between the states before and after annihilation occurs. The interpolation shows the concerted nature of the event in which four atoms are involved. The actual minimum energy path, found with NEB, shows a more complex behavior. Initially, the interstitial atom executes a hop very similar to the collinear interstitialcy mechanism describing isolated interstitial diffusion, with the saddle point geometry appearing very similar to that mechanism. Once the system passes over the saddle point, the three remaining atoms are moved by two successive interstitialcy hops, but the process is all downhill once the saddle has been cleared. There are no barriers for the subsequent hops. Thus, although the minimum energy path shows a sequence of three, seemingly independent hops, this is actually a single concerted event with

TABLE V. The energy barriers and event time scales for some of the typical defects observed in the collision cascades.

No. in cluster	species	barrier (eV)	event time at 300 K (s)	note
1	Mg_i	0.32	10^{-8}	
1	V_{Mg}	2.12	10^{21}	
1	O_i	0.40	10^{-7}	
1	V_O	2.00	10^{21}	
2	$(MgO)_i$	0.75	0.1	
		0.66	0.01	DFT
2	V_{MgO}	2.49	10^{27} ,	V_O hop,
		0.99	10^3	V_{Mg} catch up
2	V_{MgO}	2.53,	10^{27} ,	V_{Mg} hop,
		1.03	10^3	V_O catch up
3	$(MgOMg)_i$	0.59	10^{-4}	diffusion
		1.23		rotation
3	$(OMgO)_i$	0.61	10^{-4}	diffusion
		1.27		rotation
4	$(2Mg2O)_i$	1.68	10^{15}	
6	$(3Mg3O)_i$	0.24,	10^{-9}	metastable state
		0.33	10^{-8}	metastable state, DFT
		1.04	100	ground state
8	$(4Mg4O)_i$	0.66	0.01	metastable state
		1.70	10^{15}	ground state

one saddle point. Analysis of trajectories initiated from the saddle plane shows that this entire sequence takes place in roughly 0.5 ps.

From this and other TAD simulations, we find that, for small interstitial clusters, the migration energy tends to increase with cluster size. Isolated interstitials diffuse quickly, on the nanosecond time scale, with barriers of 0.32 eV for the Mg interstitial and 0.40 eV for the O interstitial. Di-interstitials are somewhat less mobile, diffusing on the time scale of a fraction of a second at 300 K with a barrier of 0.75 eV. As discussed below, the trend is broken for tri-interstitials, which, with a barrier of about 0.6 eV, diffuse faster than di-interstitials. However, tetrainterstitials are immobile, diffusing on a time scale of 10^8 yr. These tetrainterstitials can form when two di-interstitials meet during the diffusion process. The results of all of the TAD simulations are summarized in Table V and Fig. 11.

Tri-interstitials diffuse in a manner similar to the di-interstitial, though with a significantly lower barrier. We originally reported in Ref. 2 migration barriers of 0.79 eV and 0.80 eV for the Mg-O-Mg and O-Mg-O tri-interstitials, respectively. Those calculations used the free boundary geometry discussed above, but with the interior region consisting of $N=216$ moving atoms. More recently, we have improved upon those calculations and have found

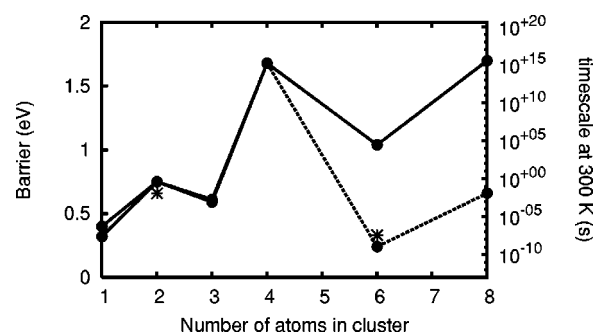


FIG. 11. Migration barriers for interstitial clusters versus cluster size. The time scale for diffusion at 300 K is also shown. The binding energy increases with the cluster size, while the energy barriers do not follow any obvious trend. The dashed line indicates barriers for metastable clusters. Asterisks indicate barriers calculated with DFT.

that the barriers are actually somewhat lower. For $N=512$ moving atoms, we find barriers of 0.59 and 0.61 eV for Mg-O-Mg and O-Mg-O, respectively. We have further tested the dependence of the diffusion barrier of Mg-O-Mg versus N . For $N=1003$, the barrier is 0.54 eV and remains essentially unchanged at $N=1731$. Thus, the value of 0.59 eV at $N=512$ is within 0.05 eV of the converged value. As with the di-interstitial structure, these tri-interstitial structures diffuse via moves in $\langle 111 \rangle$ directions, displacing three atoms from the lattice to form a new tri-interstitial via this collinear interstitialcy mechanism. For both the di- and tri-interstitials, diffusion via these $\langle 111 \rangle$ moves is isotropic; i.e., all eight $\langle 111 \rangle$ diffusion directions are accessible from a given trimer orientation.

Both di- and tri-interstitials can also rotate to a new $\langle 100 \rangle$ direction. For the di-interstitial, this rotation mechanism has a barrier of 1.20 eV. In this process, the Mg ion of the di-interstitial remains in its original $8c$ site while the O ion displaces a lattice atom, very similar to a single interstitial hop. If the O ion remains fixed instead, the barrier for this rotation is very similar at 1.24 eV. For the tri-interstitials, the corresponding mechanism has a barrier of 1.23 eV for the Mg-O-Mg tri-interstitial and 1.27 eV for the O-Mg-O tri-interstitial. In this mechanism, one of the end atoms of the tri-interstitial remains stationary while the other two atoms displace lattice atoms in a way that results in a tri-interstitial aligned along a different $\langle 100 \rangle$ axis. These rotational mechanisms do not change the isotropic diffusive character of the clusters. However, they would allow the clusters to change orientation as they approach other defects, possibly affecting cluster aggregation.

The immobility of the tetrainterstitial suggests that when clusters of four atoms form, they might act as interstitial sinks. Surprisingly, however, this is not necessarily the case. For example, the hexainterstitial, formed when a di-interstitial encounters a tetrainterstitial, is mobile, diffusing with a barrier of 1.04 eV in its ground state (100 s time scale). The structure of this ground state is shown in Fig. 9(a). More interestingly, the hexainterstitial can also exist in a metastable state, 0.89 eV above the ground state, in which it diffuses much faster. Diffusion of this metastable

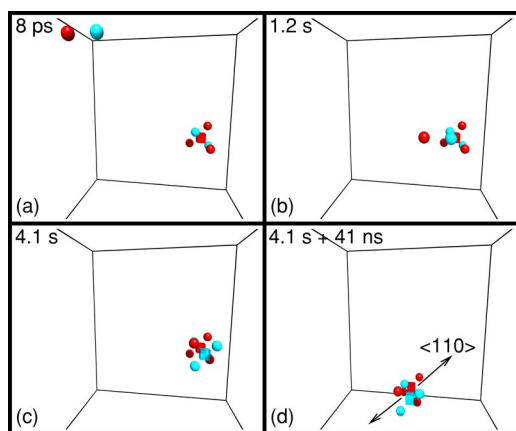


FIG. 12. (Color online) TAD simulation of the formation of a mobile hexainterstitial at 300 K. (a) A di-interstitial and tetra-interstitial begin about 1.2 nm apart. The tetra-interstitial contains four interstitial atoms, but an additional atom is displaced from its lattice site so that in this representation it appears to be composed of two Mg interstitials, three O interstitials, and one O vacancy. (b) $t = 1.2$ s; the di-interstitial has approached the immobile tetra-interstitial. (c) By $t = 4.1$ s, the combined cluster has annealed to form a persistent metastable state of the hexainterstitial. (d) This metastable form diffuses on the ns time scale with a barrier of 0.24 eV. The one-dimensional $\langle 110 \rangle$ diffusion direction is indicated. Taken from Ref. 2.

hexainterstitial occurs in two stages, with an overall barrier of 0.24 eV, but is limited to diffusion along a single $\langle 110 \rangle$ direction. At 300 K, this diffusion occurs on the nanosecond time scale. This metastable structure was found by running a TAD simulation that began with a di-interstitial and a tetra-interstitial, as illustrated in Fig. 12. When the two defects met, after some rearrangement, they formed the metastable hexainterstitial. The smallest barrier we have found to go from the metastable structure to the most stable hexainterstitial is about 1.3 eV, a process that takes years to occur at room temperature. This means that on the order of 10^{16} diffusion events will occur in the metastable state before it decays to the ground state. We do not know how often this metastable hexainterstitial will form versus the true ground state, but the fact that it did form in the single TAD simulation we performed on this di-interstitial plus tetra-interstitial encounter suggests that it will not be infrequent.

As discussed in Ref. 2, we find the behavior of the octa-interstitial is similar to that of the hexainterstitial. A metastable structure diffuses in one dimension with a barrier of 0.66 eV (0.01 s time scale), trapped by a barrier of 1.52 eV against decay to the ground state, which diffuses with the larger barrier of 1.7 eV. It is tempting to speculate that yet larger clusters may also have interesting kinetic properties. The structure of the ground state of the octa-interstitial, as described above and shown in Fig. 9(b), can be viewed as an extension of the hexainterstitial structure. One can imagine placing two hexainterstitials in adjacent cells and then removing any atoms which overlap. Such a construction gives the octa-interstitial structure.

Finally, TAD simulations have also revealed that, as interstitial defects approach vacancies, annihilation occurs via

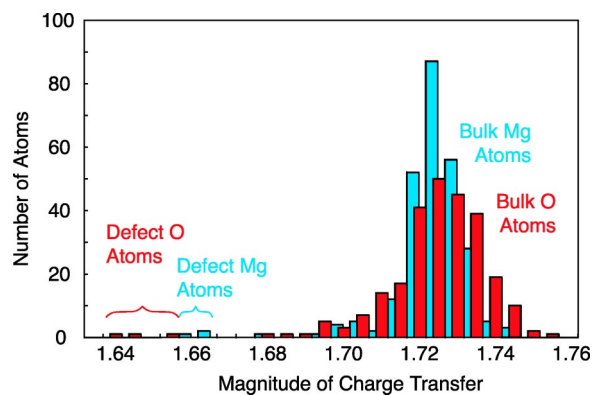


FIG. 13. (Color online) Bader decomposition of the DFT charge transfer in and around the metastable hexainterstitial cluster, relative to an isolated atom. In the bulk, each Mg atom has a net charge of 1.72 while each O atom has a net charge of -1.72 , illustrated by the peak in the charge transfer (the location of the O values have been shifted slightly to higher charge transfer for clarity). The atoms in the metastable hexainterstitial cluster, labeled in the figure, transfer slightly less charge than the bulk.

long-range concerted events. In the case of a di-interstitial close to a vacancy, many atoms are involved in the transition which eventually annihilates part or all of the di-interstitial [see Figs. 10(e) and 10(f)]. Concerted events are also important in the diffusion of interstitial clusters, with the diffusion mechanism for the metastable hexainterstitial involving 12 atoms. That is, the metastable hexainterstitial diffuses via an interstitialcy mechanism in which all six atoms composing the cluster displace and replace six atoms in the lattice; these six displaced atoms then become the hexainterstitial on the other side of the saddle point.

D. Density functional theory

Previously,² we tested some of our empirical-potential results against DFT calculations, where we found that the formation energies of the di-interstitial and metastable hexainterstitial predicted by the empirical potential agreed with the DFT calculations to within about 8%—or 0.5 eV per atom in the cluster—while the diffusion barriers for these two species agreed to within 0.1 eV. The results for the barriers are included in Fig. 11.

This is very good agreement, giving us confidence that our results are not an artifact of the potential. To understand the origin of this good agreement, we have calculated the Bader charges^{30,31} for the atoms in and around the metastable hexainterstitial configuration. In these calculations, as for those in Ref. 2, we employed the VASP code²⁸ with the PW91 functional and the projector augmented wave method²⁹ on supercells containing 216 lattice atoms and a plane wave basis with energies up to 400 eV. It was determined that a single Γ -point sampling of k space was sufficient to converge energies for this cell size. For example, increasing the k -point mesh to $2 \times 2 \times 2$ changed barrier heights by less than 0.001 eV.

The result of the Bader charge decomposition is shown in Fig. 13 in which the net charge transferred to or from each

atom in the cell is given. In the bulk, Mg atoms transfer 1.72 electrons to O atoms. This value is about 0.3 electrons less than the formal charge of 2 electrons, supporting the validity of the ionic model for this system. The atoms composing the metastable hexainterstitial transfer slightly less charge, with the least amount of charge transferred being about 1.64 electrons. Thus, the amount of charge transferred in the atoms composing the defect is very similar to the charge transfer occurring in the bulk, possibly explaining why the ionic model does so well in describing these bulk defects.

The value for the charge transferred of 1.72 is less than the full charge of 2 assumed in our model. This suggests that we might be able to improve the model by using partial charges instead of the full formal charge. This may indeed improve the ability of the potential to model certain aspects of the system, but one must take care before proceeding in this direction. Partial charge models are less transferable; a parameter set for the O-O interaction developed for MgO will be different from one developed for Al-doped MgO, for example, making comparisons of defect energies more difficult. In addition, while some properties are typically improved when a partial charge model is used, others, such as dielectric constants, can be made worse.³² Finally, the Bader charge decomposition is one of several such methods for partitioning charge. While we might expect other schemes to give qualitatively similar results, especially for the change in charge transferred among the ions in the defects, the absolute magnitude of transferred charge might differ. Thus, there is no unique value for the transferred charge to use in a partial charge model. For these reasons, while using partial charges may improve our ability to model MgO, we feel that a full charge model is more appropriate for studying a variety of complex materials.

III. DISCUSSION AND CONCLUSIONS

Combining the results from molecular dynamics, molecular statics, temperature accelerated dynamics, and density functional theory reveals an interesting picture for the room-temperature evolution of radiation damage after a low-energy cascade in MgO. Point defects and small clusters form during the first 10 ps after the impact. While vacancies are immobile at room temperature, interstitial ions diffuse quickly. They can either recombine with vacancies, effectively healing the crystal, or aggregate with other interstitials, forming successively larger interstitial clusters. These clusters become more stable with size. They also generally become less mobile with size, but there are some dramatic and important exceptions. For example, the tetrainterstitial is immobile at room temperature, but combining with a diinterstitial can give a hexainterstitial in a long-lived metastable state that diffuses faster than any other species we have observed in MgO. These mobile clusters can thus diffuse over long ranges, interacting and aggregating with clusters from other cascades which will increase the overall damage accumulation rate. In the case of the hexainterstitials and octainterstitials, the long range one-dimensional diffusion along $\langle 110 \rangle$ in their metastable states could result in an experimentally detectable signature.

As mentioned above, the potential used in this study does not account for any charge transfer between species. It is important to consider what impact this property of our model has on the results described in this work. The largest effect is in the Coulomb interactions. If charge transfer were allowed, then the charge on individual defects would be reduced and the interaction would be reduced as well. The most immediate consequence of this would be that long-range attraction between oppositely charged defects would be reduced and the time scale for, for example, annihilation would be increased. Interstitials would have to move closer to vacancies in order for there to be a high probability of recombination. There would also likely be differences in the ground state structure, as shown by density functional theory calculations,³³ and migration barriers, though the magnitude of these differences are impossible to know without direct calculation.

The impact of charge transfer on the net-neutral species we describe would likely be much less. The fact that the density functional theory calculations we have done on the di-interstitials and metastable hexainterstitials agree well with the empirical potential calculations suggests that our fully charged model describes these defects well. The DFT calculations also show that the charge transfer among atoms in the metastable hexainterstitial is similar to that in the bulk and that charge transfer does not play a big role in these neutral clusters. Thus, while the behavior we see for charged defects may not be as indicative of their behavior in real MgO, our predicted properties of neutral clusters are likely to be much more reliable.

At this point, it is difficult to directly compare our simulation results with known properties of MgO. Experimental estimates of the vacancy (likely O) migration barrier of 1.9 eV (Ref. 34) agree well with the value of about 2.1 eV predicted by this and other theoretical studies (e.g., see Ref. 36). More recent experiments find a range of activation energies for the annealing of F centers, from 1.9 to 3.4 eV.³⁵ The interpretation in those experiments is that the value of 3.4 eV corresponds to the diffusion of F centers and that lower values represent more complex mechanisms. The discrepancy between that result and ours may be due to the fact that they are examining the behavior of F^+ and F centers, while our simulations can only consider F^{++} defects at this time. However, whether F centers diffuse with a barrier of 2 eV or 3.4 eV would not change the results presented here; they would be immobile at room temperature in either case. The key result is the fast diffusivity of large interstitial clusters, which is confirmed by our DFT calculations.

Most experimental work on MgO, however, can only reveal properties of larger scale defects, such as interstitial dislocation loops and vacancy voids. We have not addressed the length scales necessary to describe these larger defects. Speculation that the $\langle 100 \rangle$ character of the larger clusters in our simulations is connected to the $\langle 100 \rangle$ growth direction of some interstitial dislocation loops is, for the moment, exactly that: speculation. In our ongoing effort, we hope to make more direct comparisons between theory and experiment.

We point out that while this study has revealed intriguing properties of defect clusters in MgO, it is not a comprehensive study of all small defects in MgO. We have not exam-

ined, for example, the properties of the pentainterstitial, nor some of the other possible small-cluster coalescence processes. Rather, we have focused on the characteristic of defects seen in low-energy cascades. Future work will expand on this.

In summary, combining MD cascade simulations, static energy minimization, temperature accelerated dynamics, and DFT, we find that it is possible to study the radiation damage properties of MgO on time scales relevant to experiment. Complex events are important, and higher level mod-

els should account for them in order to simulate the correct damage evolution.

ACKNOWLEDGMENTS

We acknowledge helpful discussions with F. Montalenti, G. Pacchioni, J. H. Harding, and D. J. Harris. This work was supported by the United States Department of Energy, Office of Science, Office of Basic Energy Sciences, Division of Materials Sciences and Engineering.

*Permanent address: Department of Mathematical Sciences, Loughborough University, LE11 3TU, UK.

- ¹D. J. Bacon and T. D. de la Rubia, *J. Nucl. Mater.* **216**, 275 (1994).
- ²B. P. Uberuaga, R. Smith, A. R. Cleave, F. Montalenti, G. Henkelman, R. W. Grimes, A. F. Voter, and K. E. Sickafus, *Phys. Rev. Lett.* **92**, 115505 (2004).
- ³D. R. Olander, *Fundamental Aspects of Nuclear Reactor Fuel Elements*, Technical Information Center, Office of Public Affairs, Energy Research and Development Administration (DOE, Springfield, VA, 1976).
- ⁴C. Kinoshita and S. J. Zinkle, *J. Nucl. Mater.* **233–237**, 100 (1996).
- ⁵W. J. Weber, R. C. Ewing, C. R. A. Catlow, T. D. de la Rubia, L. W. Hobbs, C. Kinoshita, H. Matzke, A. T. Motta, M. Nastasi, E. K. H. Salje, E. R. Vance, and S. J. Zinkle, *J. Mater. Res.* **13**, 1434 (1998).
- ⁶K. E. Sickafus, L. Minervini, R. W. Grimes, J. A. Valdez, M. Ishimaru, F. Li, K. J. McClellan, and T. Hartmann, *Science* **289**, 748 (2000).
- ⁷M. R. Sørensen and A. F. Voter, *J. Chem. Phys.* **112**, 9599 (2000).
- ⁸A. F. Voter, F. Montalenti, and T. C. Germann, *Annu. Rev. Mater. Sci.* **32**, 321 (2002).
- ⁹G. V. Lewis and C. R. A. Catlow, *J. Phys. C* **18**, 1149 (1985).
- ¹⁰R. A. Buckingham, *Proc. R. Soc. London, Ser. A* **168**, 264 (1938).
- ¹¹J. F. Ziegler, J. P. Biersack, and U. Littmark, *The Stopping and Range of Ions in Solids* (Pergamon Press, New York, 1985), Vol. 1.
- ¹²W. T. Rankin and J. A. Board, Jr., *Proceedings, 1995 IEEE Symposium on High Performance Distributed Computing p 81* (1995).
- ¹³B. Park, W. J. Weber, and L. R. Corrales, *Nucl. Instrum. Methods Phys. Res. B* **166–167**, 357 (2000).
- ¹⁴R. Smith, *Atom and Ion Collisions in Solids and at Surfaces* (Cambridge University Press, Cambridge, 1997).
- ¹⁵F. Montalenti, M. R. Sørensen, and A. F. Voter, *Phys. Rev. Lett.* **87**, 126101 (2001).
- ¹⁶G. Henkelman, B. P. Uberuaga, and H. Jónsson, *J. Chem. Phys.* **113**, 9901 (2000).
- ¹⁷G. Henkelman and H. Jónsson, *J. Chem. Phys.* **113**, 9978 (2000).
- ¹⁸G. Henkelman and H. Jónsson, *J. Chem. Phys.* **111**, 7010 (1999).
- ¹⁹F. Montalenti and A. F. Voter, *J. Chem. Phys.* **116**, 4819 (2002).
- ²⁰N. F. Mott and M. J. Littleton, *Trans. Faraday Soc.* **34**, 485 (1932).
- ²¹M. Leslie, SERC Daresbury Laboratory Tech. Report No. DL/SCI/TM31T., 1982 (unpublished).
- ²²*Computer Simulation of Solids*, edited by C. R. A. Catlow and W. C. Mackrodt (Springer-Verlag, Berlin, 1982).
- ²³E. A. Kotomin and A. I. Popov, *Nucl. Instrum. Methods Phys. Res. B* **141**, 1 (1998).
- ²⁴D. J. Bacon, F. Gao, and Y. N. Osetsky, *Nucl. Instrum. Methods Phys. Res. B* **153**, 87 (1999).
- ²⁵G. Busker, M. A. van Huis, R. W. Grimes, and A. van Veen, *Nucl. Instrum. Methods Phys. Res. B* **171**, 528 (2000).
- ²⁶T. Brudevoll, E. A. Kotomin, and N. E. Christensen, *Phys. Rev. B* **53**, 7731 (1996).
- ²⁷R. A. Evarestov, P. W. M. Jacobs, and A. V. Leko, *Phys. Rev. B* **54**, 8969 (1996).
- ²⁸G. Kresse and J. Hafner, *Phys. Rev. B* **47**, 558 (1993); **49**, 14 251 (1994); G. Kresse and J. Furthmüller, *Comput. Mater. Sci.* **6**, 16 (1996); *Phys. Rev. B* **55**, 11 169 (1996).
- ²⁹G. Kresse and J. Joubert, *Phys. Rev. B* **59**, 1758 (1999); P. E. Blöchl, *ibid.* **50**, 17 953 (1994).
- ³⁰R. F. W. Bader, *Atoms in Molecules—A Quantum Theory* (Oxford University Press, Oxford, 1990).
- ³¹G. Henkelman, A. Arnaldsson, and H. Jónsson (unpublished).
- ³²R. W. Grimes (unpublished).
- ³³E. A. Kotomin, P. W. M. Jacobs, N. E. Christensen, T. Brudevoll, M. M. Kuklja, and A. I. Popov, *Defect Diffus. Forum* **143–147**, 1231 (1997).
- ³⁴C. Kinoshita and K. Hayashi, *Adv. Ceram.* **10**, 490 (1985).
- ³⁵A. I. Popov, M. A. Monge, R. González, Y. Chen, and E. A. Kotomin, *Solid State Commun.* **118**, 163 (2001).
- ³⁶P. W. M. Jacobs, E. A. Kotomin, N. E. Christensen, and T. Brudevoll, *Mater. Sci. Forum* **239–241**, 391 (1997).